JET–P(99)47

L C Ingesson et al

Comparison of Basis Functions in Soft X-ray Tomography and Observation of Poloidal Asymmetries in Impurity Density

JET–P(99)47

Comparison of Basis Functions in Soft X-ray Tomography and Observation of Poloidal Asymmetries in Impurity Density

L C Ingesson, H Chen[1,2], P Helander[3], M J Mantsinen[4].

JET Joint Undertaking, Abingdon, Oxfordshire, OX14 3EA, UK.
[1]Also at: Imperial College, London, SW7 2BZ, UK.
[2]Present address: Lawrence Livermore National Laboratory, P O Box 808, Livermore, CA94551, USA.
[3]UKAEA/Euratom Fusion Association, Culham Science Centre, Abingdon, Oxon, OX14 3DB, UK.
[4]Also at Helsinki University of Technology, Association Euratom–TEKES, Finland.

Preprint of a Paper published in
Plasma Physics and Controlled Fusion **42** (2000) 161-180

February 2000

ABSTRACT

Natural basis functions (NBF), also known as natural pixels in the literature, have been applied in tomographic reconstructions of soft x-ray (SXR) measurements in the JET (Joint European Torus) tokamak. The results are compared with those obtained with local basis functions (LBF), and those obtained with a conventional constrained-optimization tomography method. Truncated singular value decomposition is used as the inversion method. Reconstructions without *a priori* information, such as the NBF reconstructions, are, as can be expected, less good than reconstructions in which *a priori* information is used, as in the conventional method, but the reconstructions are shown to be reliable by means of phantom simulations. Reconstructions with the same number of LBFs as NBFs without *a priori* information are comparable to NBF reconstructions, although the latter seem to be somewhat better. No significant changes in results, apart from smaller reconstruction errors, are obtained if the measuring system has more regular or complete coverage than the JET SXR system. The various tomography methods are used to assess whether a newly observed in-out asymmetry in the SXR emission during the injection of nickel into an RF-heated plasma, with the peak on the inboard side, is real. A possible explanation for the asymmetry in emissivity is an increased nickel density on the inboard side as a result of an RF-induced increase of the hydrogen-minority density on the outboard side.

Classification numbers: 52.70.La, 42.30.Wb, 52.25.Vy, 52.40.Gj

1. INTRODUCTION

Most tomography methods applied to reconstruct emission profiles in fusion research are so-called series-expansion methods, in which the inversion problem is discretized by expanding the emission profile on a set of basis functions. Three types of basis functions can be applied: (1) global, (2) local and (3) natural basis functions [1].

(1) Global basis functions are functions that are non-zero over a large part of the emitting region and describe some linear property of the emission profile. Examples of global basis functions applied in tomography in fusion research are the Fourier-Zernike [2] and Fourier-Bessel [3] expansions of the Cormack method (a method applied to soft x-ray tomography).

(2) Local basis functions (LBFs) include the much-used pixels [4–6], for which the basis function is 1 inside the corresponding pixel and 0 outside, and related functions that are nonzero in a small region on a regular grid [1,7,8]. Local basis functions are versatile as they are not related to the expected shapes of the emission profile, nor are they biased by the measuring system. In fusion research usually many more local basis functions are needed to accurately describe the emission profile than there are measurements. To overcome this underdeterminedness and the ill-posed nature of the tomography problem [9], *a priori* information such as the assumption of smoothness and zero emission outside the plasma are required as regularization.

(3) Natural basis functions (NBFs), often referred to as natural pixels in the literature, were proposed by McCaughey and Andrews [10] and Buonocore *et al.* [11] as global basis functions that are related to the strips with finite width that are viewed by the measuring system, and are therefore in a certain sense ideally suited to describe the measurements by that system [11]. Because of the relation to the measuring system, the number of NBFs is approximately equal to the number of measurements, easing the requirement for *a priori* information.

Recently, NBFs have been applied successfully in single positron emission computed tomography (SPECT) [12,13], in which a tomographic image is formed of the emission from radionuclides injected into a patient. A similarity between SPECT and tomography in fusion research is that the beam widths of the imaging system are relatively large in order to achieve a good signal-to-noise ratio. An important dissimilarity is that, in general, many more measurements from a regular coverage are available in SPECT. However, in modern soft x-ray tomography diagnostics on fusion devices there may be sufficient information (number of measurements) to make reasonable reconstructions by means of NBF methods without (or with much less) *a priori* information. The purpose of this paper is to investigate whether this is the case and to discuss the advantages and disadvantages of NBF methods compared with other tomography methods with LBFs. A number of NBFs are investigated: the original NBFs [11], generalized NBFs [14], and orthonormal NBFs [15]. Two-dimensional emission tomography without refraction and reabsorption of radiation is assumed, although in some cases reabsorption can be included in the formalism [13]

The structure of this paper is as follows. Section 2 introduces the various NBFs and LBFs and describes the numerical implementation of the tomography methods. Examples of the NBFs are given for the soft x-ray (SXR) system on the JET tokamak. The JET SXR system consists of 5 nearly complete views of the plasma with 35 or 36 channels each and one half view [figure 1(a)], all in one poloidal cross-section. The performance of the tomography methods with the various NBFs and LBFs has been assessed for the same system by means of simulations, as is discussed in section 3. A more detailed description of the numerical implementation of the NBFs and of the phantom simulations is given in reference 16. In section 4 an application is discussed in which the small amount of *a priori* information required in NBF methods was beneficial to ascertain whether a poloidal asymmetry in SXR emission is likely to be real or a result of the *a priori* information. The observed asymmetry in an RF-only heated discharge peaks on the inboard side, which is in contrast with the peaking on the outboard side usually observed in rapidly rotating plasmas with neutral-beam injection. To the knowledge of the authors this is the first time that such a peaking on the inboard side has been observed. Section 5 summarizes the results.

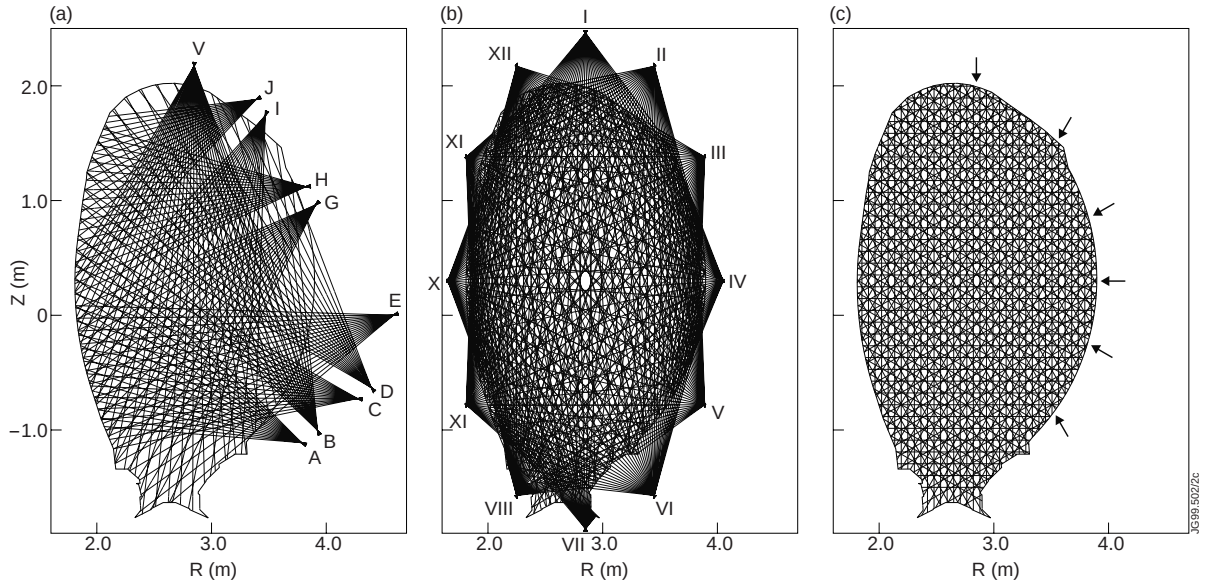

Fig.1: Average lines of sight of real and virtual imaging systems drawn in a poloidal cross-section with respect to the inner wall of the JET tokamak. (a) The JET SXR imaging system. Eight detector arrays with 18 channels are grouped in pairs to give nearly complete views of the plasma (AB, CD, GH, and IJ), one array (E, 18 channels) views half of the plasma, and one array (V, 35 channels) has a complete view. (b) A virtual fan-beam system with 12×40 lines of sight (views I–XII); views I–VI were used for simulations with 6×40 lines of sight. (c) Virtual lines of sight that correspond to 6×36 generalized NBFs used in combination with the JET SXR system (the arrows indicate the viewing directions at six angles). In the simulations with 6×40 and 12×40 lines of sight more generalized NBFs were used: 6 and 12 angles with 40 NBFs each, respectively.

2.MATHEMATICAL BACKGROUND

2.1 Series-expansion methods

In series-expansion methods the emission profile $g(x,y)$, where x and y are the spatial Cartesian coordinates, is expanded on a set of basis functions $B_j(x,y)$:

$$g(x,y) \approx \sum\nolimits_j B_j(x,y)\,\tilde{g}_j, \tag{1}$$

where $\tilde{g}_j$ are the expansion coefficients. As explained in the introduction, these basis functions can be local, global or natural. Later, the xy coordinates will be identified with the coordinates of a poloidal tokamak cross-section R and Z, respectively, and will be used interchangeably with these. The measurement of detector i can be written as

$$f_i = \{\mathsf{K}g(x,y)\}_i = \iint K_i(x,y)\,g(x,y)\,\mathrm{d}x\,\mathrm{d}y \tag{2}$$

where the integral is over the support of $g(x,y)$, which is assumed to be bounded. Here, a discrete-continuous integral operator $\mathbf{K}$ that maps the continuous function $g(x,y)$ in $\mathbf{R}^2$ to the discrete measurements f_i has been introduced. The kernel $K_i(x,y)$ describes the geometric properties of the measuring system and will be referred to as the geometric function. The function $K_i(x,y)$ is non-zero in a strip-shaped region [see fig.2(a) for an example]. Substituting equation (1) into (2) gives the matrix equation

$$\boldsymbol{f} = A\tilde{\boldsymbol{g}} \tag{3}$$

where $\boldsymbol{f}$ and $\tilde{\boldsymbol{g}}$ are vectors with elements f_i and $\tilde{g}_j$, respectively, and the matrix elements are given by

$$A_{ij} = \iint K_i(x,y)\, B_j(x,y)\, \mathrm{d}x\, \mathrm{d}y. \tag{4}$$

The mathematical description of series-expansion methods in terms of discrete-continuous operators and continuous basis functions is useful when an analytical expression for $K_i(x,y)$ can be given (for example a constant value within a strip), as is sometimes the case in the literature [12,14]. In many actual measuring systems, such as ours, the width of the strips varies with distance from the detector, and, consequently [17], the value of $K_i(x,y)$ decreases with distance [figs.2(a)and 3(a)]. In such a case the analytical evaluation of equation (4) is difficult, even if an approximate analytical expression for $K_i(x,y)$ exists, and it is most convenient to discretize $K_i(x,y)$, which we will do now. See reference 15 for an equivalent description in terms of discrete-continuous operators.

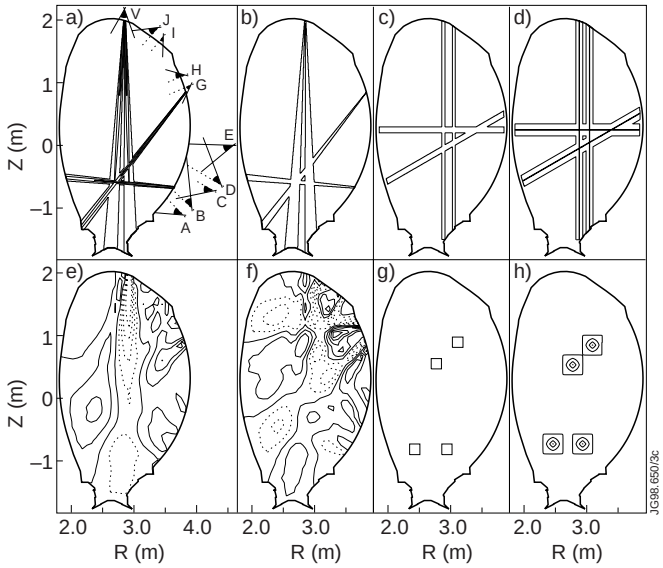

Fig.2: Contour plots of various typical basis functions drawn in a poloidal cross-section with respect to the inner wall of the JET tokamak. The NBFs are based on the SXR system at JET. (a) Four standard NBFs B^1, equal to $K_i(x,y)$. (b) Four support NBFs B^2. (c) Four constant regular NBFs B^3. (d) Four triangular regular NBFs B^4. (e,f) Two orthonormal NBFs B^5 (dotted contours indicate negative values). (g) Four square constant LBFs B^6. (h) Four pyramid LBFs B^7. Neighbouring basis functions were not drawn (see fig.3), note however that neighbouring basis functions in (d) and (h) overlap, and also in (a) and (b) in so far as $K_i(x,y)$ of neighbouring channels overlap. The representation of the basis functions in (a–d,g,h) is on the fine 400×800 grid, whereas (e,f) are on a coarser grid. In (a) also all fans of the SXR system are indicated.

We discretize $g(x,y)$, $K_i(x,y)$ and $B_j(x,y)$ on a very fine grid of M pixels (typically $M = 400 \times 800$) and obtain the vector $\boldsymbol{g}$, with elements g_m, and the matrices K and B, with elements K_{im} and B_{jm}, of which the rows correspond to the values of $K_i(x,y)$ and $B_j(x,y)$ in the pixels [16]. Equation (1) in matrix form is

$$g_m \approx \sum_j B_{jm}\,\tilde{g}_j\,, \text{ or } \boldsymbol{g} \approx B^{\mathsf{T}}\,\tilde{\boldsymbol{g}} \tag{5}$$

and equation (2) is

$$\boldsymbol{f} = K\boldsymbol{g}\,. \tag{6}$$

The matrix A of equation (3) in terms of the matrices K and B is $A = K\,B^{\mathsf{T}}$. An efficient way to calculate the elements of K is given in references 7 and 17.

2.2 Natural basis functions

The most straightforward choice of NBFs, which will be referred to as *standard* NBFs, is [11]

$$B^1 = K\,. \tag{7}$$

With this choice equation (5) becomes

$$\boldsymbol{g} \approx K^{\mathsf{T}}\tilde{\boldsymbol{g}} \tag{8}$$

which is symmetrical with equation (6). If one, as is customary in the tomography field, refers to the strip-like integral of equation (2) as *projection*, with the choice of NBFs one can refer to equations (1) and (5) as the *backprojection*. Indeed, equations (1) and (8) are closely related to a discrete version of the continuous backprojection operator of which the continuous form is well known in the filtered-backprojection tomography method, also called convolution backprojection, that is widely used in medical tomography [18]. For obvious reasons, the matrix $A = KK^{\mathsf{T}}$ is sometimes referred to as the projection-backprojection matrix. A contour plot of a collection of these basis functions is shown in fig.2(a) and cross-sections in fig.3(a). The contours indicate strongly varying values of B^1 inside the strips on their support (i.e. the region where they are non-zero). This is the reason why in the present application the name natural *basis function* seems preferable over the more usual name natural *pixel*. Furthermore, the name natural basis function stresses the relation with local and global basis functions.

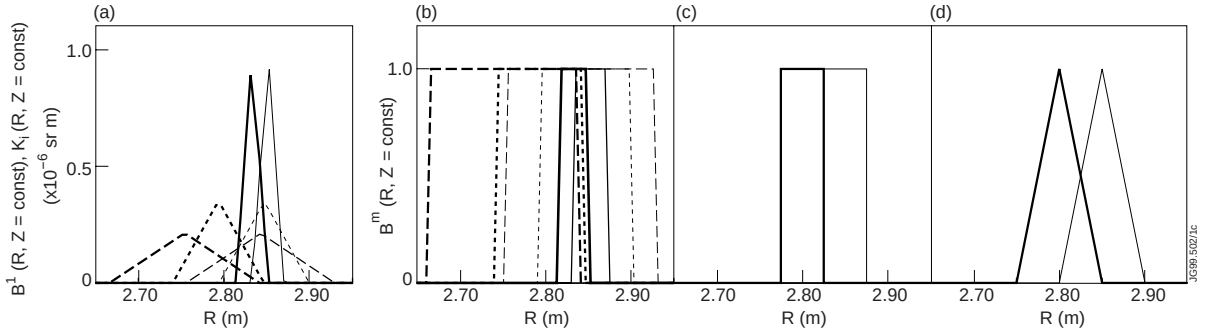

Fig.3: Cross-section of two neighbouring NBFs [similar to the vertical NBFs of figs.2(a–d)] at Z = 1.5 m (solid lines), 0.25 m (dotted lines) and –1.0 m (dashed lines). Thin and thick lines distinguish between the two neighbours. (a) $B^1(R,Z) = K_i(R,Z)$, (b) B^2, (c) B^3 and (d) B^4.

With the choice of basis functions of equation (7) the number of expansion coefficients $\tilde{g}_j$ is equal to the number of measurements *I*, so that equation (3) may have a unique solution. Ways of solving equation (3) are discussed in section 2.3. If the number of detectors is much smaller than the number of grid points *M*, it is much more efficient to solve equation (3) instead of (6), which is one of the great advantages of NBF methods. A further advantage is that NBFs are guaranteed to represent the measurements process well, and can be much better in that respect than if the geometric function has to be represented on LBFs. Disadvantages are that, in general, *a priori* information is not taken into account in NBF methods [19] and that the measurements alone may not be sufficient to accurately describe the emission profile. The latter disadvantage can be expressed more exactly as follows [1,20]: only the information about $g(x,y)$ that lies in the subspace (called measurement space) spanned by the set of all geometric functions, is contained in the measurements, and no information about the orthogonal space (called null space). This is true for any basis functions: *a priori* information is required to fill the null space. Because NBFs can only represent the information in the measurement space, *a priori* information cannot be added in a straightforward way. For a regular coverage this may not be such a problem, but for irregular coverage a significant null space may exist.

Table I: Summary of the basis functions used.

Name	**Type**	**Definition**
B^1	standard NBF	$B^1=K$
B^2	support NBF	$B^2_{jm} = \begin{cases} 1 & \text{if } K_{jm} > 0, \\ 0 & \text{if } K_{jm} = 0. \end{cases}$
B^3	regular constant NBF (generalized)	constant value within regularly spaced strips
B^4	regular triangular NBF (generalized)	triangular value within regularly spaced overlapping strips
B^5	orthonormal NBF	$B^5 \leftarrow V_K^{\mathsf{T}}$
B^6	square constant LBF	constant within square
B^7	pyramid LBF	product of two overlapping triangle functions in *x* and *y* directions

* The $I \times M$ submatrix of V_K^{T}, which is the same shape as *K*, is assigned to B^5.

Next, we introduce a number of other basis functions. The definitions are given in table I and a graphical representation is given in figs.2(b–h) and 3(b–d). The strong variation of B^1 over the strip may give rise to unwanted effects in reconstructions, in particular when neighbouring channels do hardly overlap. In such a case, NBFs that are uniform over the support of *K* may be preferable, which gives B^2 [figs.2(b) and 3(b)]. One is free in the choice of basis functions, so

one can choose the backprojection to use the backprojection operator (basis functions) of another (virtual) measuring geometry K' than in the projection K, i.e. $B = K'$ such that $A = KK'^{\mathsf{T}}$. Such basis functions have been referred too as *generalized* NBFs [14]. These NBFs may be advantageous if the coverage of the measuring system is irregular or truncated, in which case K' may be chosen to represent a (virtual) full regular measuring system, which has a smaller null space than the actual measuring system. We tried two types of generalized NBFs: parallel strips at regular angles with constant values B^3 [figs.2(c) and 3(c)] and similar regular strips with overlapping triangular values B^4 [figs.2(d) and 3(d)], with the virtual number of detectors approximately equal to the actual number of detectors, see figure 1(c).

It is evident that all NBFs defined so far are highly non-orthogonal. Orthonormal NBFs [10,15] can be obtained as follows. Given the singular value decomposition (SVD) $K = U_K S_K V_K^{\mathsf{T}}$ (see any book on matrix computations, for instance reference 21), where the subscripts indicate the matrix of which the SVD matrices are the decomposition, the basis functions (rows of B^5) are set equal to the appropriate number of rows of V_K^{T} [15]. Contour plots of two typical orthonormal NBFs for the JET SXR system are shown in figs.2(e,f). The structure of these NBFs for the SXR system are not very clear, although many contours are spread along one or more lines of sight. For a system with regular coverage much more structure can be expected [15]. It will be shown that orthonormal NBFs have limited applicability to our application.

Two sets of LBFs, the number of which is approximately equal to the number of detectors, were constructed to make possible a direct comparison of NBFs with LBFs. These LBFs are non-overlapping square constant pixels B^6 [fig.2(g)] and half-overlapping "pyramid" basis functions B^7 [fig.2(h)]. The latter are the product of one triangle function in the Z (or y) direction and one in the R (or x) direction [7], which results in a pyramid shape with rounded corners. The summation of equation (1) in the case of the pyramid LBFs results in a continuous $g(x,y)$, whereas in the case of the square constant pixels $g(x,y)$ is step-like.

2.3 Inversion

In NBF methods the tomographic reconstruction is obtained by solving equation (3) and backprojecting the solution by equation (1) or (5). The result of the tomographic reconstruction is often referred to as the tomogram. For LBFs the same procedure can be used, but in that case equations (1) or (5) describe a mere mapping in the region covered by the LBF. If equation (3) is overdetermined, i.e. there are more (known) measurements than (unknown) basis-function expansion coefficients, or the number of knowns and unknowns are the same, there may be a unique solution. However, in the presence of noise and inconsistencies in the data it is likely that there is no exact solution. It is well known that the tomography problem is a so-called ill-posed problem [9]: it is easy to see that the integral equation (2) averages over variations in $g(x,y)$ and

hence the inverse will amplify noise in the measurements $\boldsymbol{f}$ [22]. The inverse problem needs to be regularized. In the following we will assume that there are I measurements and J basis functions.

Truncated SVD (TSVD) is a reasonable way to obtain a stable solution to equation (3) when $J \approx I$ (see for instance reference 12 and references therein, and reference 22). The (truncated) pseudo-inverse or Moore-Penrose inverse of the $I \times J$ matrix A, with SVD $A = U_A S_A V_A^{\mathsf{T}}$, is given by [21]

$$A^{+} = V_A S_A^{+} U_A^{\mathsf{T}}$$

where S_A is a $I \times J$ diagonal matrix $S_A = \mathrm{diag}(s_1,\ldots,s_r)$, with $r = \min(I, J)$ and singular values $s_{1\ldots r}$, and its pseudo-inverse is the diagonal $J \times I$ matrix $S_A^{+} = \mathrm{diag}(1/s_1,\ldots,1/s_t,0,\ldots,0)$, with truncation value $t \le \mathrm{rank}(A) \le r$. The singular values are customarily sorted in descending order. Small singular values will make the inverse A^{+} unstable; this can be prevented by truncating the inverse, i.e. by choosing t suitably ($t < r$). It can be shown that the solution $\tilde{\boldsymbol{g}} = A^{+}\boldsymbol{f}$ is the least square solution if the system is overdetermined ($I \ge J$) and the minimum norm solution if the system is underdetermined ($I < J$) [21]. The SVD of A can be calculated by standard mathematical packages. It is computationally intensive, but for given K and B it only needs to be done once and the matrices U_A, S_A and V_A can be stored. Note that the matrix K, and consequently B and A, are very sparse matrices with only a few percent of non-zero values. For an efficient implementation of the NBF methods it is essential to take the sparseness into account in the algorithms.

Figure 4 shows the singular values of the projection-backprojection matrix for the various basis functions for the JET SXR system. For orthogonal NBFs (not shown in fig.4) it can be shown that the singular values are equal to the square root of those of standard NBFs (B^1). The characteristics of all NBFs and LBFs are similar: the first few singular values drop quickly, then there are more than a hundred singular values with constant slope (on a logarithmic scale) and above about 160 the values drop steeply. Small singular values, in particular after the steep drop, indicate redundancy in the information of the emission profile by the basis functions (the redundancy is due to the overlap of the support of geometric functions that correspond to crossing the lines of sight). The truncation level of the SVD should be chosen higher than where the singular values fall off too much below the noise level; the optimal choice of truncation will be discussed in connection with the simulations in section 3.1. The number of

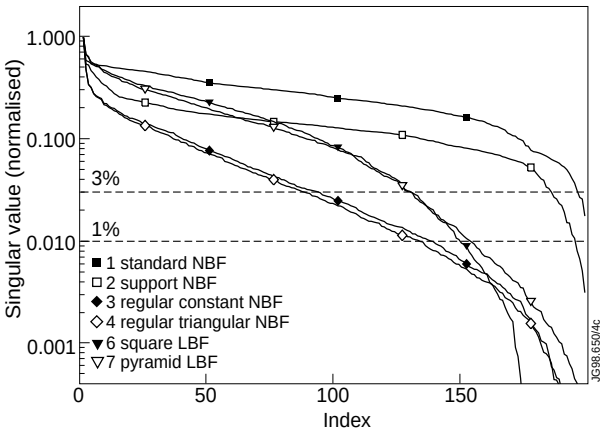

Fig.4: Singular values of the projection-backprojection matrix A *for the JET SXR system, normalized to the largest singular value. These singular values were obtained with* K *on the fine 400×800 grid.*

singular values of the matrix A that can be taken in the TSVD corresponds to the degrees of freedom, or independent pieces of information, gathered by the measuring system [10].

Because of the way K and A are related for standard and orthonormal NBFs, one can show by substituting the solution $\tilde{\boldsymbol{g}} = A^{+}\boldsymbol{f}$ into equation (5) and using the SVD of K and A and the unitary properties of U and V that the backprojected solution is equal to

$$\boldsymbol{g} = K^{+}\boldsymbol{f}\,. \tag{9}$$

The solution found with standard and orthonormal NBFs is therefore equal to the solution found if TSVD were applied to K in equation (6). The application of standard NBFs has some advantages over the direct application of TSVD as in equation (9), in particular when $K_i(x,y)$ can be expressed analytically [11,12] and when the coverage of the measuring system is regular [11,15]. Furthermore, if the number of grid basis functions required for an accurate discretization of $\boldsymbol{g}$ and K is larger than the number of measurements, as is the case in the present application, SVD of A is much more efficient (possibly by many orders of magnitude) than SVD of K; hence the NBF approach is more efficient than the solution by equation (9). In our application we do not benefit from the solution by orthonormal basis functions as the inefficient SVD of K is needed to obtain the basis functions. The orthonormal NBFs are therefore not considered any further in this paper and are only referred to in relation with the TSVD of K as in equation (9). However, the orthonormal NBFs give insight into what the actual basis functions are when one solves equation (6) by means of the TSVD of equation (9).

2.4 Constrained-optimization method

The performance of NBF and LBF methods described have been compared with the standard tomography method used for SXR and bolometer tomography at JET [7], which is here referred to as the *reference* method. This is a series-expansion method with a grid of pyramid LBFs (there are about six times more basis functions than measurements) in which the solution is found by a constrained optimization (this is equivalent to Phillips-Tikhonov regularization). The *a priori* information is given by an object function that quantifies anisotropic smoothness on flux surfaces [7,23], in other words: for the given constraints the smoothest solution is found. From the tomogram one can backcalculate what would be measured if the tomogram were the actual emission profile and compare these with the measurements. This gives the misfit σ_f between measurements f and backcalculated measurements $A\hat{\boldsymbol{g}}$:

$$\sigma_f = \frac{\left\| A\tilde{\boldsymbol{g}} - f \right\|}{\left\| f \right\|} \tag{10}$$

where the bars indicate the Euclidean norm. The constraint in the constrained optimization method is given by the so-called discrepancy principle [24], i.e. the solution is found for which the misfit equals the estimated errors ε in the measurements. The main parameter in the constrained

optimization method is given by the estimated errors; other parameters specify the exact form of the object function. Other, similar tomography methods applied to SXR tomography, and tomography in other wavelength ranges on fusion devices, often use square pixel basis functions, and isotropic smoothness, flatness, smoothness weighted by the emissivity, or maximum entropy as object function [4–6,25,26].

3. COMPARISON OF METHODS

3.1 Description of simulations

The performance of tomography methods can be compared by means of phantom simulations. Phantoms are assumed emission profiles, which are used to calculate pseudo-measurements, i.e. what the detectors would measure if the phantom were the true emission profile. The tomographic reconstruction of the pseudo-measurements can be compared with the phantom. The NBF and LBF methods described are compared in phantom simulations with the reference method.

In the numerical implementation of the tomography methods which use TSVD of A, a grid of 400×800 square pixels was used, which will be referred to as the fine grid. This grid was chosen sufficiently fine so that the geometric functions $K_i(x,y)$ could be accurately represented.The tomograms are shown on this fine grid. The reference method (as stated above) and TSVD of K used a coarser grid with about 1200 grid points, referred to as coarse grid, because the fine grid is not feasible with these methods as they require the SVD of the matrices $K^{\mathsf{T}}K$ and K, respectively. The representations on the coarse grid are not necessarily worse than the fine grid as the phantoms are given on the coarse grid. However, it is found (section 3.2) that for the LBF and NBF the fine grid gives reconstructions closer to the phantom than the coarse grid, which means that for those methods the fine grid is more adequate.

Three phantoms, listed in table II, were used in the simulations. Phantom I [fig.6(a)] is based on actual SXR measurements reconstructed by the reference method (JET discharge 40305; see Sec. 4 for more details). Because the reference method is known to smooth the result, the

Table II: Tomogram reconstruction errors σ_g (in per cent) for phantom simulations. The best results on each row are indicated in bold.

System	Phantom	Ref.[a]	NBF 1	NBF 2	NBF 3	NBF 4	(NBF 5)[a]	LBF 6	LBF 7
JET	I experim. crescent	8.0	45.9	34.6	28.4	26.8	33.8	28.7	**21.3**
JET	II Gaussian	3.5	63.9	34.0	22.0	**18.0**	46.5	41.6	27.1
JET	III ring	27.1	61.5	43.4	40.5	36.7	45.2	40.7	**29.0**
6×40	I	9.1	23.6	22.7	24.0	22.0	24.6	23.3	**17.4**
12×40	I	5.5	17.8	16.5	21.1	19.7	23.1	21.5	**15.9**

[a] On a coarser grid

peaks of the phantoms were enhanced. Phantoms II and III are mathematical inventions that are not likely to occur in a plasma, but that give insight into what happens if there are steep gradients in the emission profile. Phantom II is a peaked Gaussian emission profile and III is a ring with a Gaussian cross-section. More detailed simulation results with more phantoms are described in reference 16; those results lead to the same conclusions obtained here with three phantoms.

In the simulations a realistic level of noise is added to the pseudo-measurements; in the present simulations that is Gaussian noise with a standard deviation of 3% relative to the pseudo-measurement. Tomographic reconstructions g (the tomogram) of the pseudo-measurements can be compared directly with the phantom g_0 to give the tomogram error

$$\sigma_g = \frac{\|g - g_0\|}{\|g_0\|}.$$

The tomogram error is an objective quality measure, with a global minimum, that can be optimized by varying the reconstruction parameters, i.e. the estimated misfit ε in constrained optimization or the number of singular values (expressed in relative terms by s_t/s_1) in TSVD. The misfit σ_f [equation (10)] is also a quantitative error measure. Contrary to σ_g, it is usually a monotonic function of the estimated misfit ε in constrained optimization or the number of singular values in TSVD. Figures 5(b–h) show that in the TSVD σ_g has a minimum for a value of s_t/s_1 that is close to the noise level for the methods for which there are very small singular values (B^3, B^4, B^6 and B^7), whereas for methods for which all singular values are relatively large the best result is obtained with no or little truncation (B^1, B^2 and B^5). It is well known that [9] the minimum σ_g in constrained-optimization methods that use the discrepancy principle is often for an ε that is slightly smaller than the noise level [fig.5(a)]. Other objective quality measures can be defined, such as the amount of negative values in the tomogram (all tomography methods used in this report can result in unphysical negative emissivity values), but the tomogram error was adequate for our purpose. The image of the tomogram also gives an impression of the quality of the reconstruction. Although this is

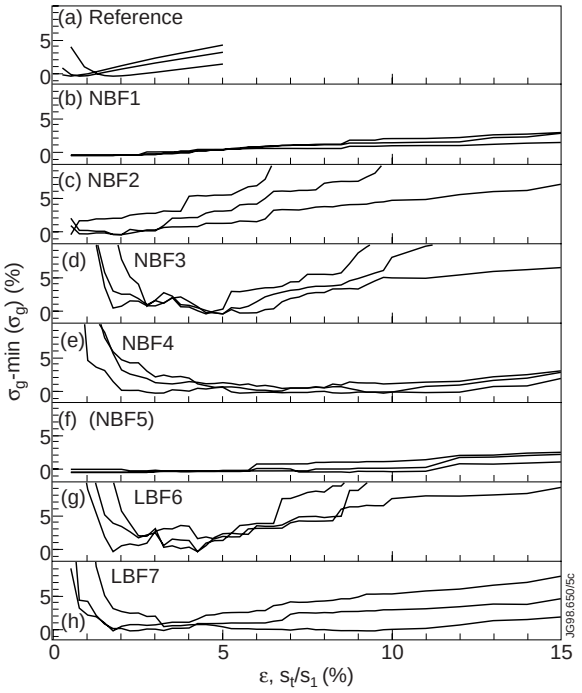

Fig.5: Tomogram errors $\sigma_g - \min(\sigma_g)$ for the three phantoms (the three curves in each graph) as a function of ε [in (a)] and s_t/s_1 [in (b–h)] for tomographic reconstructions on the fine 400×800 grid for the various tomography methods indicated, except (f) which was done by TSVD of the matrix K *on the coarse grid. The value of* $\min(\sigma_g)$ *can be found in table II.*

not an objective quality measure, it can play an important role in deciding which method gives the best results. The tomograms of the simulation are discussed in detail next.

3.2 Simulation results

The reconstruction errors in fig.5 and the minimum reconstruction errors in table II show that results of the various phantoms are the same qualitatively, i.e. the relative performance of the various tomography methods does not depend much on the phantom [16]. Therefore, only tomograms of the phantom simulations with phantom I are discussed in detail (fig.6).

Figure 6(b) shows that the reference method gives a reconstruction that is very similar to the phantom [fig.6(a)], but that the peak and the hollow have been somewhat smoothed, as can be expected when using a regularization based on smoothness. The NBFs B^1 [fig.6(c)] do not give a good reconstruction, with high values at the edge, because the basis functions have a triangular shape and neighbours do not overlap. Still, the crescent shape is discernible. The NBFs B^2 [fig.6(d)] perform better because the supports of the geometric functions of the detectors of a camera fill the region well. However, due to the irregular coverage by the system, one gets unrealistic gaps between viewing directions. The NBFs B^3, which correspond to a virtual system with regular coverage, alleviate this problem and the reconstruction is better [fig.6(e)]. The "cubist" features of the reconstruction, i.e. sharp edges, can be rounded by smoothing the image, which gives a very acceptable result [fig.6(f)]. A smooth result is also obtained by using triangular regular NBFs [B^4, fig.6(g)], which give the best result of the types of NBF tested. Straightforward TSVD of the matrix K on the coarse grid, which mathematically corresponds to the orthonormal NBFs B^5, also leads to a reasonable reconstruction [fig.6(h)], but of a lesser quality than obtained with the reconstructions on the fine grid (cf. table II). The reconstruction with square LBFs B^6 [fig.6(i)] also shows the main features, but for all phantoms the reconstruction is worse than that with NBFs B^3 and B^4, and sometimes worse than reconstructions with NBFs B^2. This is in agreement with what has been found in the literature [11,12]. The smoother reconstruction with pyramid LBFs B^7 [fig.6(j)] is better. In fact, its tomogram error is lower than for any of the NBFs for most phantoms. The relatively large size of the basis functions is clear from the large number of local minima and maxima. Although the reconstructions with NBF B^4 are not free from artefacts, they seem preferable to the reconstructions with B^7 despite the somewhat larger tomogram error, in particular because the hollowness and values on the left side of the crescent are reconstructed better and because it is smoother. The reason for the tomogram error being larger for the NBFs seem to be the non-zero features at the edge of the plasma, while such features are suppressed for LBF B^7 because the basis functions go to zero in many places close to the edge. The very small tomogram error for the reference method is achieved because the *a priori* information fits the smooth phantoms very well. Although for less smooth phantoms the

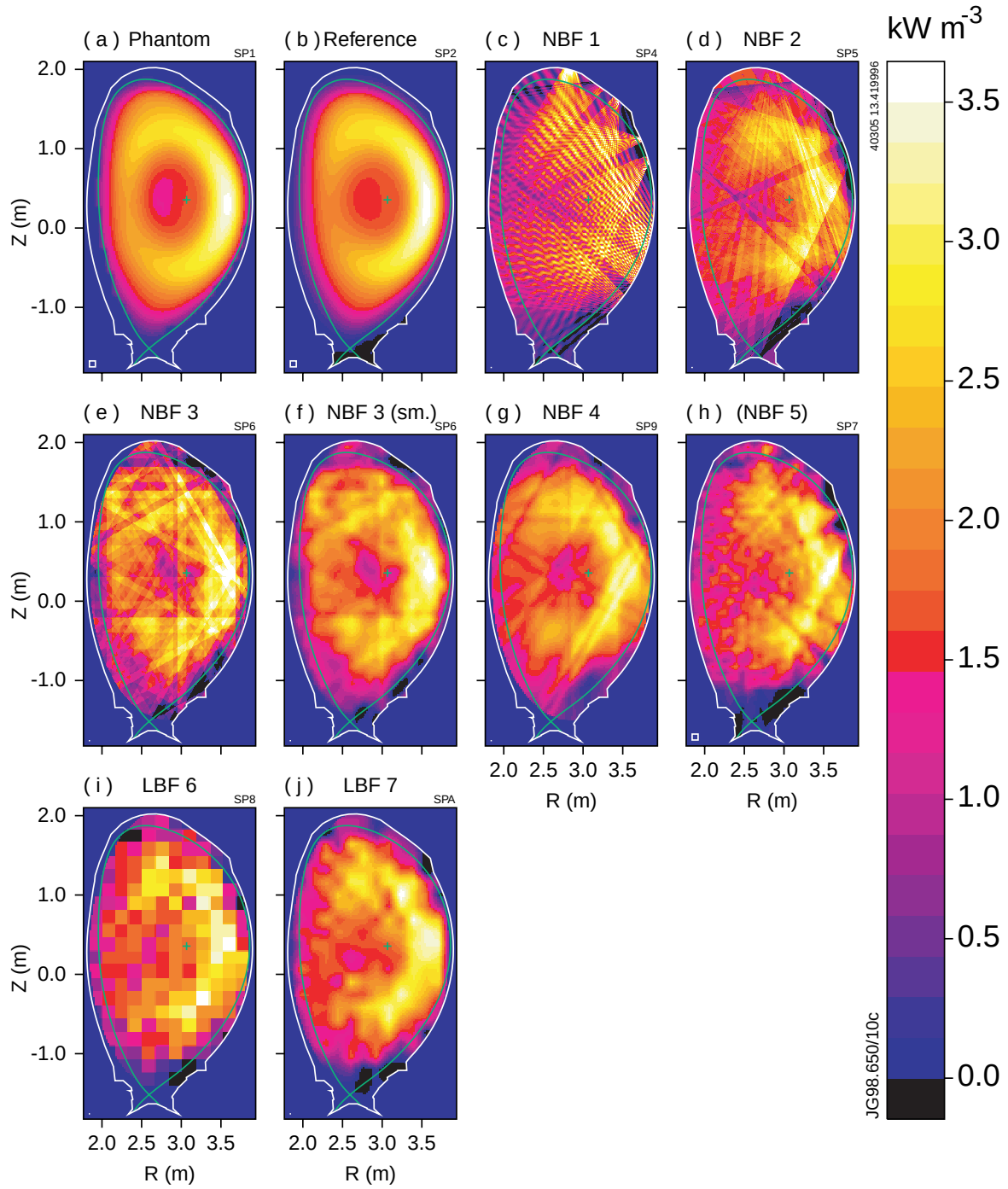

Fig.6: (a) Phantom I. (b–j) Tomographic reconstructions by the various methods: (b) reference method, (c–g) NBFs, (h) TSVD of the matrix K *on the coarse grid and (i,j) LBFs. Image (f) was derived from image (e) by smoothing. The green curve indicates the magnetic separatrix in the plasma and the box in the lower left corner the grid size.*

tomogram error is larger, it is smaller than in the NBF and LBF reconstructions since in those significant method-dependent artefacts appear, whereas the reference method gives less-pronounced artefacts.

Some of the artefacts in fig.6(c-g) can clearly be attributed to the irregular coverage of the channels and the shapes of the geometric functions. One can therefore ask, whether better results can be obtained with NBFs if the coverage is more regular. One can also wonder whether the good performance of NBFs reported in the literature is due to the much larger number of channels in those applications. To address the first question, simulations have been carried out with a virtual system with approximately the same number of channels as the JET SXR system, but spaced in a regular way: six fans at regular angles over 180° with 40 channels each, where each fan covers the entire plasma cross-section [see fig.1(b)]. To address the second question, six additional virtual fans were added on the outboard of the tokamak vessel to give a total of 12x40 channels spread over 360°. Because the qualitative results for the various phantoms in the simulations with the JET SXR system were the same, the simulations with the virtual systems were only carried out for phantom I. The number of NBFs B^3 and B^4 and LBFs B^6 and B^7 was increased according to the number of channels available in the virtual systems. The results are given in table II. Surprisingly, the reconstruction with the reference method for the 6x40 system is somewhat worse than that with the JET SXR system. The reconstruction for the 12x40 system, however, is significantly better. It is clear that the NBF methods perform much better with the regular systems. For the 12x40 system NBFs B^1 and B^2 even outperform NBFs B^3 and B^4, indicating that (1) the problems for the JET SXR system were purely due to limitations in that system and (2) for regular systems it is better to use normal NBFs based on the geometric function than generalized NBFs based on a virtual regular system. However, the LBFs also perform better for the regular systems and the tomogram errors for LBFs B^7 are still somewhat better than the tomogram errors with NBFs. One could think that the results with the 12x40 system are better than with the 6x40 system partly because there are more basis functions, which can achieve a better fit to the phantom. It was verified that there is no direct relation between the number of basis functions and the reconstruction error by reconstructing the pseudo-measurements of the 6x40 system with B^4 and B^7 for the 12x40 system (so there are roughly twice as many basis functions as measurements). The reconstruction error σ_g for B^4 was 20.6%, i.e. better than with the 6x40 system for both measurements and basis functions (see table II), but worse than the 12x40 system for both. The reconstruction error σ_g for B^7 was 18.5%, thus worse than with the basis functions of the 6x40 system.

4. APPLICATION

In-out asymmetries of impurity radiation have often been observed in tokamak plasmas [7,27,28]. The asymmetries are most pronounced for heavy impurities such as trace nickel injected by laser ablation, but can also occur with intrinsic impurities, as is the case in Phantom I [fig.6(a)]. Phantom I is a time slice (at 13.42 s into ELMy H-mode JET discharge 40305) in a plasma with a high toroidal rotation velocity (of the order of 500 km s^{-1}) induced by neutral beam injection

(NBI). Impurities accumulate in the plasma, but they do not necessarily reach the centre on a short time scale. The radiation by the impurity ions can be as large as the background bremsstrahlung and recombination radiation. The in-out asymmetry of the crescent-shaped emission profile can be explained very well in quantitative terms by the centrifugal force experienced by the impurity ions that is caused by the rapid toroidal rotation due to NBI [29–31]. In plasmas with (unbalanced) NBI heating the peak in radiation is therefore always on the outboard side of the poloidal cross-section, which at JET has been observed in ELMy and ELM-free H-mode plasmas [32], as well as in optimized-shear plasmas [33]. Here, an asymmetry in SXR emission with the peak on the inboard side is discussed.

4.1 Assessment of in-out asymmetry with peak on inboard side

The in-out asymmetry with the peak at the inboard side, which is considerably smaller than the asymmetry discussed above, has been observed in a JET plasma after nickel injection during RF heating only, see fig.7(a). The observed SXR radiation is mainly line and recombination radiation of the Ni^{26+} charge state. In this discharge the toroidal rotation is only $25\ \mathrm{km\ s^{-1}}$, compared to typically $600\ \mathrm{km\ s^{-1}}$ in NBI heated plasmas. The discharge is similar to so-called optimized-shear discharges [34]: it has a wide region of low shear, with safety factor on axis $q_0 \approx 1.5$. The nickel is injected in the pre-heating phase and there is only a weak internal transport barrier (ITB) for electron heat transport as the heating power (3 MW) is considerably below the threshold for a strong ITB for ion heat transport. When the ion ITB is weak, the impurities reach the centre of the plasma in about 50 ms [33].

It has been assessed whether the observed asymmetry is likely to be real, or to be the result of artefacts in the tomographic reconstruction. Artefacts in a tomographic reconstruction can

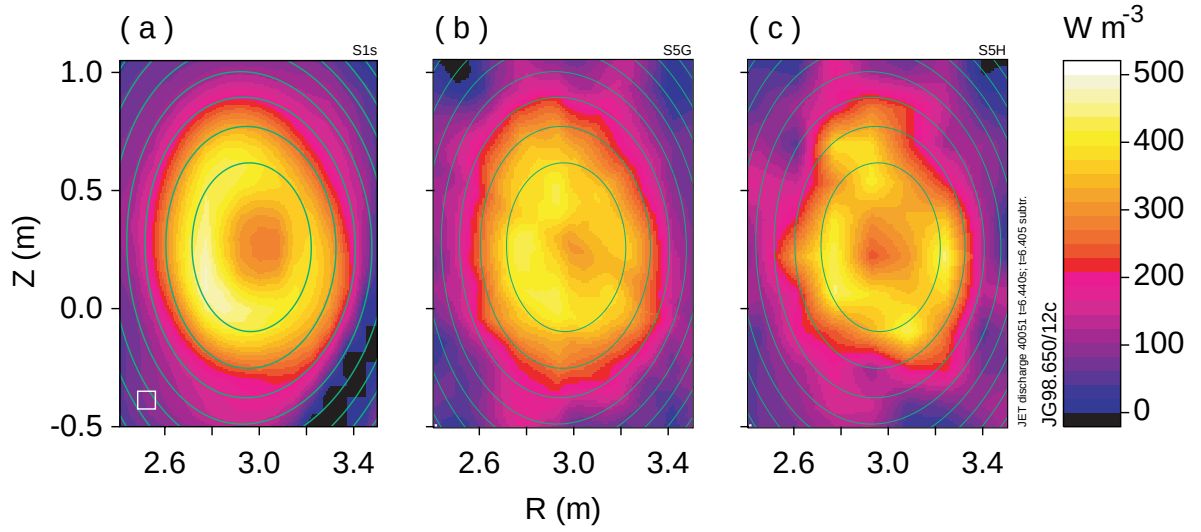

Fig.7: Background subtracted tomographic reconstructions of SXR emission after nickel injection into a discharge with RF-heating only (JET discharge 40051). Only the central part of a poloidal cross-section is shown, and a number of flux surfaces are drawn. (a) Reference method. (b) NBF B[4]. (c) LBF B[7]. The results with least apparent artefacts (after varying the reconstruction parameters) are shown.

result (1) from uncertainties in the measurements (e.g. noise and calibration errors), (2) from the tomography algorithm in combination with asymmetric coverage by the measuring system, or (3) from incorrect *a priori* information.

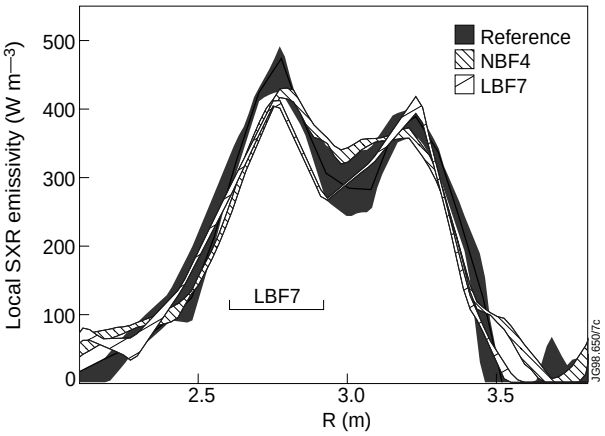

Fig.8: Horizontal cross sections at the magnetic axis of fig.7. The regions of uncertainty were obtained by varying the reconstruction parameters within reasonable limits. The extent of the LBF B^7 is indicated by a horizontal bar.

(1) The reliability of the tomographic reconstruction can be analysed by varying reconstruction parameters within reasonable limits [7]. This analysis (grey region in fig.8), which included varying the estimated noise and calibration factors in the measurements and to a limited extent varying the assumptions in the *a priori* information, revealed that there is little doubt that the observed in-out asymmetry is real.

(2) Phantom simulations with symmetric phantoms have revealed that with the JET SXR system, which has a relatively dense coverage on the outboard side and a coarse coverage on the inboard side, asymmetric artefacts tend to increase the reconstructed radiation on the outboard side, thus contrary to the asymmetry in fig.7(a).

(3) As said, the variations in assumptions in the *a priori* information were limited (a comparison was made between the assumption of isotropic smoothness and varying degrees of anisotropic smoothness on flux surfaces), and thus it would be very beneficial to compare fig.7(a) with reconstructions that do not assume *a priori* information (apart from the truncation level in the TSVD). Figures 7(b) and (c) show the reconstructions with B^4 and B^7, respectively. The phantom simulations described in section 3 give an indication for each type of basis function of what is a reasonable range of truncation level s_t/s_1 for reconstructions of actual measurements (in which case σ_g cannot be determined as no phantom exists to compare with). Within this the truncation level can be optimized to give the reconstruction with the least apparent artefacts. Although individually fig.7(b) and (c) can only give an indication about details in the emission profile, taken together they confirm that the asymmetry is real. For B^4 this is also clear in the cross-section in fig.8, but for B^7 it is not evident from the cross-section because at this particular cross-section the coarseness of the basis functions (indicated in fig.8 by a bar) impedes an adequate representation in every single point. Figures 7(a)–(c) also consistently show a slight up-down asymmetry with the peak downwards in the ion $\mathbf{B}\times\nabla|\mathbf{B}|$ direction. We will not discuss the up-down asymmetry further and concentrate on the in-out asymmetry. See, for instance, references 35 and 36 for discussions on up-down asymmetries in impurity density in tokamak plasmas.

4.2 A possible explanation for the in-out asymmetry

As already mentioned, neoclassical theory predicts poloidal density asymmetries as a result of toroidal rotation [30,31]. In the tokamak edge, where the plasma is sufficiently collisional and the radial gradients are very steep, recent neoclassical theory also predicts poloidal asymmetries produced by friction forces arising from poloidal rotation [35]. This mechanism is predicted to cause heavy impurities to accumulate on the inboard side of each flux surface, as observed in the present experiments. However, in the plasma core the collisionality is so low — the nickel is in the plateau transport regime whereas the deuterium is in the collisionless regime — that such asymmetries should be small. The comparison between theory and experiment is slightly complicated by the lack of a measurement of poloidal rotation and of the ion temperature and density profiles (charge-exchange spectroscopy does not give these values without NBI beams). If the latter are assumed to be of the same order of magnitude as the electron values, the asymmetry caused by poloidal friction is predicted to be many orders of magnitude smaller than observed. Therefore this theory cannot explain the present observations. Neoclassical theory also predicts an up-down asymmetry [35,36], which again is caused by the ion-impurity friction and tends to be very small in the JET core plasma.

We propose that the ion-cyclotron resonance heating may be responsible for the in-out asymmetry in the present experiment. The RF-heating scheme applied is hydrogen-minority heating in a deuterium plasma, with multiple resonances at major radii R = 3.0–3.2 m (i.e. slightly on the outboard side). Code calculations show that most RF power (89%) is absorbed by hydrogen, and much less than 1% by Ni^{26+} (which has a second-harmonic resonance slightly on the inboard side), thus making a direct effect of heating of nickel an unlikely explanation for the observed asymmetry. The remaining power is absorbed by electrons, deuterium and impurities. It is well known that the heating can give rise to a poloidal asymmetry in the density of minority ions since these particles tend to be trapped on the outside of the torus and the turning points of their orbits drift towards the resonance layer due to the heating. This RF-produced accumulation of minority ions on the outboard side can lead to a corresponding impurity accumulation on the inboard side by the following mechanism.

In the plasma, the density n_a of each particle species a with charge Z_a is normally expected to follow the electrostatic potential ϕ according to a Boltzmann distribution

$$n_a = n_{a0} \exp\left(-\frac{Z_a e\phi}{T_a}\right) \approx n_{a0}\left(1-\frac{Z_a e\phi}{T_a}\right) \tag{11}$$

so that the poloidal variation of the density is $\tilde{n}_a / n_{a0} = -Z_a e\phi / T_a$, while the temperature T_a is approximately constant on the flux surface. The subscript 0 indicates the density where $\phi = 0$ and the tilde the variation on the flux surface. Equation (11) follows, for instance, from the parallel momentum equation

$$n_a Z_a \nabla_{/\!/} \phi + T_a \nabla_{/\!/} n_a = 0$$

where we have neglected inertia, assumed that the rotation is slow, and we have also disregarded parallel temperature variations and parallel friction, assuming that the collision frequency is reasonably small. As discussed in reference 35, this condition is satisfied if

$$\frac{Z^2 qR}{\Omega_{\mathrm{i}} \tau_{\mathrm{ii}} L_\perp} << 1$$

where τ_{ii} is the bulk ion collision time, Ω_{i} the ion gyrofrequency, q the safety factor, and $L_\perp$ the radial scale length of the density and temperature profiles. This criterion is practically always satisfied in the JET core plasma, even if the impurities are in the plateau or Pfirsch-Schlüter regime in the usual sense of neoclassical theory. If we take the plasma to consist of electrons (e), bulk ions (D), heavy impurities (Z), and RF-heated minority ions (H), we expect that all species except the minority ions should be Boltzmann distributed, because the dynamics of the latter is strongly influenced by the RF heating. Quasineutrality requires

$$n_{e0}\left(1+\frac{e\phi}{T_e}\right) - n_{\mathrm{D0}}\left(1-\frac{e\phi}{T_{\mathrm{i}}}\right) - Z n_{Z0}\left(1-\frac{Ze\phi}{T_{\mathrm{i}}}\right) = n_{\mathrm{H0}} + \tilde{n}_{\mathrm{H}}$$

where the temperature of the impurities and bulk ions is equal to T_{i}. We may normalize ϕ so that $n_{\mathrm{D0}} + n_{\mathrm{H0}} + Z n_{\mathrm{Z0}} - n_{e0} = 0$, and then solve for the poloidal variation of the impurity density, which gives

$$\frac{\tilde{n}_Z}{n_{Z0}} = -\frac{Ze\phi}{T_Z} = -\frac{Z\tilde{n}_{\mathrm{H}}/n_{\mathrm{D0}}}{1+\frac{T_{\mathrm{i}}}{T_e}+\frac{n_{Z0}Z^2}{n_{\mathrm{D0}}}} \qquad (12)$$

where we have assumed $n_{\mathrm{D0}} \approx n_{e0}$. Note that the poloidal variation in the impurity density has opposite sign to that of the minority ions. The accumulation of the latter on the outboard side gives rise to an electric field that pushes the other ion species to the inboard side. For highly charged impurities, such as nickel, this effect is amplified by their large charge Z. On the other hand, the density of electrons and bulk ions is nearly constant on each flux surface. Equation (12) is valid even if there are several charge states present of the same impurity, as long as its concentration is small enough that it may be regarded as a trace impurity.

Figures 7 and 8 shows the SXR emissivity after nickel injection from which the background emission profile, i.e. without nickel emission, has been subtracted. The radiation profile of figure 7 can therefore be assumed to be purely due to nickel radiation, predominantly line and recombination radiation of the Ni^{26+} charge state, which is approximately proportional to the electron density and Ni^{26+} density. As stated, only high-Z ions are affected significantly by the hydrogen asymmetry. Therefore, it can be concluded that the 10% asymmetry in SXR emissivity is caused by a similar asymmetry in the Ni^{26+} density. With a hydrogen concentration of about

2%, equation (12) implies that $\tilde{n}_{\mathrm{H}}/n_{\mathrm{H0}} \approx 10\% - 30\%$ is sufficient to explain the observed asymmetry. Next it is shown that the RF heating can cause such an asymmetry in hydrogen density.

Using the measured background plasma parameters as input, the heating has been simulated by the PION code [37], which calculates the power deposition and evolution of the pitch-angle averaged velocity distribution functions of resonating ions self-consistently, and the FIDO code [38], which uses a Monte-Carlo method to solve the three-dimensional orbit-averaged Fokker-Planck equation with the wave parameters and power deposition profile given by PION. Figure 9 shows the results of the simulations of the FIDO code, extended to handle multiple frequencies, in the form of a scatter plot of hydrogen ions in phase space $(\hat{\Psi}_\phi, \hat{\lambda})$, dimensionless variables and orbit classification introduced in reference 39. In the simulations the distribution function has evolved for approximately one slowing-down time. The region of trapped particles is region VII. There are more trapped particles with $\hat{\lambda} < 0$, i.e. with turning points on the outboard side, than trapped particles with $\hat{\lambda} > 0$, i.e. with turning points on the inboard side. Note also the significant population of ions in region VIII, i.e. co-passing particles on outboard side. According to these simulations 53% of the total hydrogen population consists of either trapped hydrogen ions with turning points on the outboard side or of co-passing ions on the outboard side. This is significantly higher than the population of trapped hydrogen ions with turning points on the inboard side (18%). Therefore, a considerable in-out asymmetry in the hydrogen ion density is to be expected, which is sufficient to account for the in-out asymmetry in the nickel density. The remaining 29% of the hydrogen ion population are mainly passing particles in region I and do not contribute significantly to the in-out asymmetry.

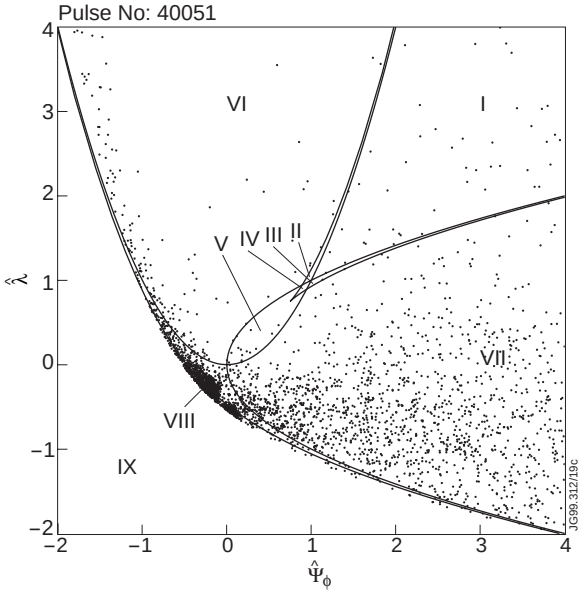

Fig.9: Orbit classification of a representative number of particles in the FIDO Monte-Carlo simulation in $(\hat{\Psi}_\phi, \hat{\lambda})$ space. The regions are numbered according to reference 39.

In neoclassical transport theory [30,31] the radial impurity transport is influenced by poloidal asymmetries, whether the poloidal asymmetry is caused by the centrifugal force from toroidal rotation, poloidal friction, or by other mechanisms such as the one considered here. Therefore, it is of some interest to accurately diagnose such asymmetries before the accuracy of theories for radial impurity transport can be verified quantitatively.

5. CONCLUSIONS

Natural basis functions have been applied successfully to tomography with the JET SXR system in numerical simulations. Although reconstructions with a conventional tomography method are significantly better, reconstructions with NBFs, which require less *a priori* information than the conventional tomography methods, are useful to investigate whether features of a reconstruction are real or may be due to the regularizing *a priori* information in conventional tomography methods. The NBF methods may also be a useful design tool to assess the potential of future tomography diagnostics. The simulations show that the information supplied by the number of measurement of the JET SXR system is sufficient to derive the main features of the emission profiles. Simulations with virtual systems with improved coverage or a doubled number of detectors do not lead to a different assessment of NBF tomography methods: although reconstruction errors are smaller for most methods, the conventional tomography method remains preferable. Future work includes the comparison with the maximum-entropy tomography method, which uses different *a priori* information, unbiased by model assumptions (see, for instance reference 25 for a description of the maximum entropy method).

If the coverage by the viewing system is irregular, the regular (generalized) NBFs perform better than the NBFs that describe the actual viewing system. For systems with regular coverage and optimum overlap between neighbouring channels the opposite is true. The appropriate NBFs give more accurate reconstructions than the traditional pixels (LBFs without *a priori* information). Pyramid LBFs, which describe a bilinear interpolation between grid points, give smaller reconstruction errors than NBFs for most phantoms. However, the reconstructions with pyramid LBFs have coarse artefacts, and the smoother reconstructions obtained by NBFs, which show some relevant features better, seem to be preferable, in particular in the application in section 4. The larger reconstruction errors in the NBF method may be due to relatively larger artefacts at the edge of the reconstruction region than for pyramid LBFs. It is possible to improve the generalized-NBF reconstructions by including *a priori* information, such as smoothness between the expansion coefficients of neighbouring basis functions [19], but this is outside the scope of this paper in which we attempt to minimize the influence of *a priori* information.

By using the NBF and LBF methods without *a priori* information to supply independent information supplementary to a reconstruction with the standard tomography method, it has been established beyond doubt that an in-out asymmetry in the SXR emission during nickel injection in a JET discharge with RF heating only, with the peak in emission on the inboard side, is real. An RF-induced poloidal asymmetry of the hydrogen-minority ions seems to be the most likely cause of the poloidal asymmetry in the nickel density. This application shows that, despite reconstructions of a lesser quality, NBF methods can be a useful addition to standard tomography methods that rely on *a priori* information.

ACKNOWLEDGEMENTS

We thank the members of the JET Task Force for advanced tokamak scenarios for carrying out the experiments and gratefully acknowledge valuable discussions with Drs M Romanelli and G A Cottrell. Part of this work was funded jointly by the UK Department of Trade and Industry and Euratom.

REFERENCES

[1] Hanson K M and Wecksung G W 1985 *Appl. Opt.* **24** 4028–4039

[2] Granetz R S and Smeulders P 1988 *Nucl. Fusion* **28** 457–476

[3] Nagayama Y 1987 *J. Appl. Phys.* **62** 2701–2706

[4] Holland A and Navratil G A 1986 *Rev. Sci. Instrum.* **57** 1557–1566

[5] Iwama N, Yoshida H, Takimoto H, Shen Y, Takamura S and Tsukishima T 1989 *Appl. Phys. Lett.* **54** 502–504

[6] Mlynár J 1995 *Czech. J. Phys.* **45** 799–816

[7] Ingesson L C, Alper B, Chen H, Edwards A W, Fehmers G C, Fuchs J C, Giannella R, Gill R D, Lauro-Taroni L and Romanelli M 1998*Nucl. Fusion* **38** 1675–1694

[8] Lewitt R M 1990 *J. Opt. Soc. Am A* **7** 1834–1846

[9] Turchin V F, Kozlov V P and Malkevich M S 1971 *Sov. Phys. Usp.* **13** 681–703

[10] McCaughey D G and Andrews H C 1977 *IEEE Trans Acoustics, Speech, Signal Processing* **ASSP-25** 63–73

[11] Buonocore M H, Brody W R and Macovski A 1981 *IEEE Trans. Biomed. Eng.* **BME-28** 69–78

[12] Gullberg G T and Zeng G L 1994 *IEEE Trans. Nucl. Sci.* **41** 2812–2819

[13] Gullberg G T, Hsieh Y-L and Zeng G L 1996 *IEEE Trans. Nucl. Sci.* **43** 295–303

[14] Hsieh Y-L, Gullberg G T, Zeng G L and Huesman R H 1996 *IEEE Trans. Nucl. Sci.* **43** 2306–2319

[15] Baker J R, Budinger T F and Huesman R H 1992 *Critical Reviews in Biomedical Engineering* **20** 47–71

[16] Ingesson L C 1999 *Application of natural basis functions to soft x-ray tomography* to be published as JET Report JET-R(99)07 (Abingdon, UK: JET Joint Undertaking)

[17] Ingesson L C, Böcker P J, Reichle R, Romanelli M and Smeulders P 1999 *J. Opt. Soc. Am. A* **16** 17–27

[18] Lewitt R M 1983 *Proc. IEEE* **71** 390–408

[19] Ingesson L C "A tomographic reconstruction method with generalized natural basis functions and *a priori* information" submitted to *Inverse Problems*

[20] Hanson K M and Wecksung G W1983 *J. Opt. Soc. Am.* **73** 1501–1509

[21] Golub G H and Van Loan C F 1996 *Matrix computations 3rd Ed.* (Baltimore: Johns Hopkins University Press) pp 256

[22] Hansen P C 1992 *Inverse Problems* **8** 849–872
[23] Fuchs J C, Mast K F, Hermann A and Lackner K 1994 *Proceedings of the 21st EPS Conference on Controlled Fusion and Plasma Physics,*ed Joffrin E *et al*, Europhysics Conference Abstracts Vol 18B (EPS), Part III, pp 1308–1311
[24] Bertero M, De Mol C and Pike E R1988 *Inverse Problems* **4** 573–594
[25] Ertl K, Von der Linden W, Dose V and Weller A 1996 *Nucl. Fusion* **36** 1477–1488
[26] Anton M, Weisen H, Dutch M J, Von der Linden W, Buhlmann F, Chavan R, Marletaz B, Marmillod P and Paris P 1996 *Plasma Phys. Control. Fusion* **38** 1849–1878
[27] Smeulders P 1986 *Nucl. Fusion* **26** 267–273
[28] Giannella R, Christensen M, De Angelis R, Gottardi N, Lauro-Taroni, L Mattioli M and Pasini D 1992 in *Proceedings of the 1992 International Conference on Plasma Physics* ed Freysinger W *et al*, Europhysics Conference Abstracts Vol 16C (EPS), Part I, pp 279–282
[29] Wesson J A 1997 *Nucl. Fusion* **37** 577–581
[30] Helander P 1998 *Phys. Plasmas* **5** 1209–1211
[31] Romanelli M and Ottaviani M 1998 *Plasma Phys. Control. Fusion* **40** 1767–1773
[32] Giannella R, Chen H, Alper B, Coffey I, Cottrell G A, Gormezano C, Hawkes N C, Ingesson L C, Lauro-Taroni L, Peacock N J, Sips A C C, Söldner F, Tubbing B and Zastrow K-D 1997 in *Proceedings of the 24th EPS Conference on Controlled Fusion and Plasma Physics* ed Schittenhelm M *et al*, Europhysics Conference Abstracts Vol 21A (EPS), Part I, pp 53–56
[33] Chen H, Coffey I, Giannella R, Hawkes N C, Ingesson L C, Lauro-Taroni L, Lawson K, O'Mullane M G, Romanelli M, Peacock N J, Von Hellermann M and Zastrow K-D 1998 in *Proceedings of the 1998 International Conference on Plasma Physics*, ed Pavlo P, Europhysics Conference Abstracts Vol 22C (EPS), pp. 1947–1950
[34] The JET Team (presented by Söldner F X) 1997 *Plasma Phys. Control. Fusion* **29** B353–B370
[35] Helander P 1998 *Phys. Plasmas* **5** 3999–4004
[36] Rice J E, Terry J L, Marmar E S, Bombarda F 1997 *Nucl. Fusion* **37** 241–249
[37] Eriksson L-G, Hellsten T and Willén U 1993 *Nucl. Fusion* **33** 1037–1048
[38] Carlsson J, Hellsten T and Eriksson L-G 1996 *FIDO, a code for computing the resonant-ion distribution function during ICRH* Report ALF-1996-104 (Stockholm, Sweden: Royal Institute of Technology)
[39] Porcelli F, Eriksson L-G and Berk H L 1994 in *Proceedings of the 21st Conference on Controlled Fusion and Plasma Physic*, ed Joffrin E *et al*, Europhysics Conference Abstracts Vol 18B (EPS), Part II, pp. 648–651